Monthly Notices
of the
ROYAL ASTRONOMICAL SOCIETY

MNRAS **435,** 2391–2406 (2013) doi:10.1093/mnras/stt1448
Advance Access publication 2013 August 29

# A possible formation scenario for dwarf spheroidal galaxies – II. A parameter study

P. Assmann,[1,2]★ M. Fellhauer,[1]★ M. I. Wilkinson,[3] R. Smith[1] and M. Blaña[1]

[1]*Departamento de Astronomía, Universidad de Concepción, Casilla 160-C, Concepción, Chile*
[2]*Departamento de Astronomía, Universidad de Chile, Camino El Observatorio 1515, Las Condes, Santiago, Chile*
[3]*Department of Physics & Astronomy, University of Leicester, University Road, Leicester LE1 7RH, UK*

Accepted 2013 August 2. Received 2013 June 20; in original form 2013 January 31

## ABSTRACT

Dwarf spheroidal (dSph) galaxies are considered the basic building blocks of the galaxy formation process in the Lambda cold dark matter hierarchical cosmological model. These galaxies are believed to be the most dark matter (DM) dominated systems known, have the lowest stellar content and are poor in gas. Many theories attempt to explain the formation of dSph galaxies resorting to the fact that these galaxies are mainly found orbiting large galaxies or invoking other mechanisms of interactions. Here, we show the full set of simulation as an extension of our fiducial model, where we study the formation of classical dSph galaxies in isolation by dissolving star clusters within the DM halo of the dwarf galaxy. In our parameter survey, we adopt cored and cusped DM halo profiles and consider different numbers of dissolving star clusters. We investigate the dependence of observable quantities with different masses and scalelengths of the DM halo and different star formation efficiencies. We find that our proposed scenario explains many features of the classical dSph galaxies of the Milky Way, like their morphology and their dynamics. We see trends how the surface brightness and the scalelength of the luminous component vary with the parameters of our simulations. We also identify how irregularities in their shape, i.e. clumpiness and ellipticity vary in our simulations. In velocity space, we identify the parameters leading to flat velocity dispersions curves. We recognize kinematically cold substructures in velocity space, named fossil remnants and stemming from our unique initial conditions, which alter the expected results. These streaming motions are considered as a key feature for future observation with high resolution to validate our scenario.

**Key words:** methods: numerical – galaxies: dwarf – galaxies: star clusters: general – galaxies: star formation – galaxies: structure.

## 1 INTRODUCTION

Dwarf spheroidal (dSph) galaxies have sparked great interest in astronomy in the latest years, since they would be the seed of the formation of larger structures in the cold dark matter (CDM) cosmology. They are believed to be highly dark matter (DM) dominated objects. The observed dSph galaxies are characterized by low surface brightnesses with an absolute magnitude ranging within $-13 \leq M_V \leq -9$ (Mateo 1998; Belokurov et al. 2007), half-light radii from 40 to 1000 pc (Mateo 1998; Simon & Geha 2007; Martin, de Jong & Rix 2008), low central concentrations and old stellar populations in almost all cases. Their mass in stars is low (less than $10^8$ $M_\odot$) and (with the exception of Leo T; see Irwin et al. 2007; Ryan-Weber et al. 2008) they are devoid of H I gas (Grcevich & Putman 2009). However, due to their intrinsic faintness the study of dSph galaxies has been very difficult.

During the past decade, in the era of Sloan Digital Sky Survey and large spectroscopic surveys with 8-metre-class telescopes, our understanding about these objects in our Local Group has grown substantially. New dSph galaxies have been found, doubling the sample of the nine dSphs that we already knew (Willman et al. 2005; Belokurov et al. 2006, 2007; Sakamoto & Hasegawa 2006; Zucker et al. 2006; Irwin et al. 2007; Walker et al. 2007). Furthermore, several known dSph galaxies (e.g. Fornax, Sculptor, Sextans, Ursa Minor) show signs of stellar substructure or multiple distinct chemo-kinematic populations (Bellazzini, Ferraro & Pancino 2001; Mackey & Gilmore 2003; Coleman et al. 2004, 2005; Kleyna et al. 2004; Walker et al. 2006; Battaglia et al. 2008, 2011). Specifically, in Fornax it is observed, that there are stellar overdensities along the minor axis and five globular clusters, possibly remnants of past mergers (Mackey & Gilmore 2003; Coleman et al. 2004, 2005) or an unknown formation mechanism. Although enormous advances

★ E-mail: passmann@astro-udec.cl (PA); mfellhauer@astro-udec.cl (MF)

in measuring and understanding the properties of these faint objects are made, there is not a definitive model of a possible formation scenario that can predict all the known properties.

There are many models that attempt to explain the possible formation of these dSphs (Kormendy & Bender 2012). One class considers the DM cosmology as a starting point, assuming dwarf disc galaxies embedded in DM haloes as initial models. To convert these objects into the dSph galaxies we know, external processes have to be invoked. These external influences could stem from a larger galaxy (e.g. like the Milky Way, MW), exerting tidal and ram pressure stripping forces (e.g. Einasto et al. 1974; Faber & Lin 1983; Gnedin, Hernquist & Ostriker 1999; Mayer et al. 2001, 2006, 2007; Kravtsov, Gnedin & Klypin 2004; Klimentowski et al. 2009; Kazantzidis et al. 2011; Del Popolo 2012) on to the dwarf. In these models, the morphological transformation by tidal forces of late-type dwarfs, leading to objects resembling present-day dwarf irregular (dIrr), combined with mass-loss due to tidal and ram pressure stripping aided by heating due to the cosmic ionized background can turn the dwarfs into objects with low angular momentum, high mass-to-light ratios, faint stellar luminosity profiles and velocity dispersion profiles that resemble classical dSph galaxies. These models have difficulties to explain the presence of distant isolated dSph galaxies such as Tucana and Cetus.

Another mechanism considers resonant stripping (introduced by D'Onghia et al. 2009). The models start with the same initial conditions as described above, i.e. they start with rotationally supported galaxies, but this time consider resonant stripping by encounters between dwarf disc galaxies. The dSph galaxies are formed by a process driven by gravitational resonances.

There is another model that attempts to explain the formation of these dwarf galaxies, without assuming DM haloes at all, i.e. leaving the standard cosmological framework. The model is based on energy and momentum conservation, when gas-rich galaxies interact (Metz, Kroupa & Jerjen 2007). In this model, the dSph galaxies are regarded as second-generation objects, devoid of DM, forming in the tidal tails of gas-rich interacting galaxies.

All the models cited above consider the interaction between two or more galaxies to explain the formation of dSph galaxies. Here, we present a different approach, considering pieces of observational evidence for kinematic substructures (Willkinson et al. 2002). These properties are consistent with the kinematics of disrupted star clusters (SCs), i.e. stellar streams.

We investigate, numerically, initial conditions for isolated models that allow for the formation of objects that resemble the classical dSph galaxies. Our model is based on the assumption that stars never form in isolation but in a clustered way like associations and SCs (Tutukov 1978). The dynamical evolution of these SCs, i.e. their dissolution due to gas expulsion and subsequent formation of a diffuse stellar distribution in the centre of a DM halo, may explain the formation of classical dSph galaxies, including all their irregularities in the stellar and kinematic distribution as well as surviving SCs around them. We envisage that our scenario could be immediately relevant for forming dSphs from initial conditions similar to Leo T which has low luminosity, little evidence of angular momentum in its gas component (Ryan-Weber et al. 2008) and show no signs of being perturbed by the tidal forces from nearby galaxies (i.e. the MW in the case of Leo T).

In our first paper (Assmann et al. 2013), we introduced our scenario, showed and discussed the results of a fiducial model, which matches the observations of classical dSph galaxies. We also presented possible ways to verify our scenario. In this paper now, we show how our results depend on the initial conditions of our simulations by performing a wide parameter search.

## 2 SETUP

### 2.1 DM haloes

One of the parameters we choose for testing our formation scenario is the profile of the DM halo. We consider two profiles for the DM – cusped and cored. Standard, DM-only cosmological simulations suggest that galaxy haloes should have cusped inner profiles (see e.g. Navarro, Frenk & White 1997, hereinafter NFW). We generate initial conditions for our cusped NFW haloes using NEMO, which is described in Dehnen & McLaughlin (2005). On the other hand, we note that dynamical models of several Local Group dwarf galaxies suggest that these galaxies may have DM haloes with cored profiles (Kleyna et al. 2003; Goerdt et al. 2006; Gilmore et al. 2007; Cole et al. 2012). Further, there is also evidence from the stellar kinematics for the presence of cored profiles in these objects (Battaglia et al. 2008; Walker & Peñarrubia 2011). Therefore, we also consider models with a cored DM halo using a Plummer profile (Plummer 1911). Both types of DM halo profiles are modelled using 1000 000 particles.

We adopt two variable parameters related with the DM halo. The first one is the mass enclosed within 500 pc, $M_{500}$. The second is the scalelength $R_{\rm h}$ of the DM halo. We consider masses $M_{500} = 10^7$, $4 \times 10^7$ and $10^8\,{\rm M}_\odot$. For each mass, we further investigate three different scalelengths for the DM halo. We adopt $R_{\rm h}$ equal to 0.25, 0.5 and 1.0 kpc.

The corresponding virial radii $R_{\rm vir}$ and concentration parameters $c = R_{\rm vir}/R_{\rm h}$ for the NFW haloes can be found in Table A1.

### 2.2 Luminous component

The luminous components of our simulations are formed by the evolution of many ($N_0$) SCs within the DM halo. We model each SC as a Plummer sphere (Plummer 1911), following the recipe of Aarseth, Henon & Wielen (1974). The Plummer radius, $R_{\rm pl}$, is 4 pc and the cut-off radius, $R_{\rm cut}$, is 25 pc. The values for $R_{\rm pl}$ and $R_{\rm cut}$ are based on the observations of young SCs in the Antennae galaxy (Whitmore et al. 1999). All SCs are represented by 100 000 particles each.

There are many processes acting on SCs, for example gas-expulsion, stellar evolution, relaxation, external tidal fields. However, gas-expulsion can be considered the most important. From the observations in Antennae galaxy, Fall (2006) found that the number of clusters drop exponentially with age and that the median age of clusters is only $10^7$ yr. In addition, in the MW, Lada & Lada (2003) speculate that only a small fraction of embedded clusters (10 per cent) can become open clusters. Motivated by these facts, we add the process of gas-expulsion to our model and we study how the results are affected considering different values of star formation efficiency (SFE) for the SCs.

We implement this process in the following way.

(i) We assume a final total luminous mass of the dSph galaxy of $4.5 \times 10^5\,{\rm M}_\odot$. These value lies in the range of stellar masses of the classical dwarfs (Mateo 1998).

(ii) This mass is now divided into $N_0$ SCs giving a final mass of a single cluster. For simplicity, we assume that all SCs have the same mass and do not take a mass spectrum into account.

(iii) Now we adopt an SFE and alter (i.e. increase) the mass of a single cluster according to its mass in the embedded phase, i.e. mass of stars and gas. In this form, we set up the embedded cluster as a Plummer sphere in virial equilibrium.

(iv) After starting the simulation, we mimic the gas-expulsion by reducing the mass of the SC during one of its crossing-times back to the mass of the stars alone, leaving the cluster out of virial equilibrium and slowly dissolving.

In the simulations, we vary the initial number of SCs within the DM halo and the SFE. We consider an initial number, $N_0$, of 15, 30 and 60 SCs. These numbers have been chosen arbitrarily.

The star formation rate and efficiency in a dSph galaxy is supposedly low (Bressert et al. 2010). Therefore, we adopt values of SFE of 15 and 30 per cent for each SC. But we also check if a high value of the SFE, i.e. 60 per cent, allows the formation of an object that resembles a dSph galaxy.

The SCs are placed inside the DM halo following a Plummer distribution. We choose this distribution, taking into account the fact that we expect more SCs to form in the central area than further out in the dwarf. The initial number of clusters is that low, that the exact form of the distribution is not of importance, as different distributions could not be differentiated due to low number statistics. Initially, these SCs are in virial equilibrium on their orbits inside the DM halo. The initial orbital velocities are obtained using the Jeans equation (see Binney & Tremaine 1987):

$$\sigma^2_{r,i}(r) = \frac{1}{\rho_i(r)} \int_r^{rc} \frac{G M_{\rm tot}(r')}{r'^2} \rho_i(r')\, {\rm d}r', \quad (1)$$

where $M_{\rm tot}$ corresponds to the total mass given by the sum of the mass of all embedded clusters and the mass of the DM halo in each simulation.

As the mass of the halo is much higher than the mass of the expelled gas, we do not consider the lost gas-mass in our simulations, apart from its effect on the SCs, which is leaving them out of virial equilibrium and dissolving.

The distribution of the SCs has a scalelength, $R_{\rm sc}$, which we vary to be 250, 500 and 1000 pc.

In Table 1, we show the nomenclature that we use to label each simulation. The first column specifies what type of DM halo profile we are using. N is used to refer to an NFW profile and P to a Plummer profile. The second column indicates the number of SCs at the beginning of each simulation, where 015, 030 and 060 correspond to 15, 30 and 60 SCs, respectively. The next two columns are used to denote the mass enclosed at the radius of 500 pc and the scalelength of the DM halo, respectively. For an example, M 407 is used to denote that $M_{500} = 4.0 \times 10^7\,{\rm M}_\odot$ and RH 025 that $R_h = 0.25$ pc. Similarly, the fifth column denotes the scalelength of the initial distribution of the SCs, $R_{\rm sc}$. In the sixth column, we indicate the SFE: 15, 30 and 60 per cent.

A more detailed view of the initial conditions of all our simulations can be found in Table A1.

**Table 1.** Table explaining the labels of all our simulations. The first column specifies what type of DM halo profile we are using. N is used to refer to an NFW profile and P to a Plummer profile. The second column indicates the number of SCs at the beginning of each simulation, where 015, 030 and 060 correspond to 15, 30 and 60 SCs, respectively. The next two columns are used to denote the mass enclosed at the radius of 500 pc and the scalelength of the DM halo, respectively. For example, M 407 is used to denote that $M_{500} = 4.0 \times 10^7\,{\rm M}_\odot$ and RH 025 that $R_h = 0.25$ pc. Similarly, the fifth column denotes the scalelength of the initial distribution of the SCs. In the sixth column, we indicate the SFE: 15, 30 and 60 per cent.

| N/P | $N_0$ | $M_{500}$ | $R_{\rm h}$ | $R_{\rm sc}$ | SFE |
|---|---|---|---|---|---|
| N | 015 | M 107 | RH 025 | RS 025 | S15 |
| P | 030 | M 407 | RH 050 | RS 050 | S30 |
| | 060 | M 108 | RH 100 | RS 100 | S60 |

### 2.3 The simulations

As described above we start our simulations with all components in virial equilibrium. All SCs are inserted at the same time for simplicity. This does not imply that our models depend on the fact that a dSph galaxy has just a single star formation episode. It just reduces the number of free parameters. We leave the investigation of more complicated forms of star formation histories to a follow-up project.

Within the first internal crossing-time of the SCs, we remove their assumed gas-mass by artificially reducing the mass of each particle. This leaves the cluster out of equilibrium, expanding and slowly dissolving along its orbit inside the DM halo.

The simulations are performed using the particle-mesh code SUPERBOX (Fellhauer et al. 2000), which has additional two levels of high-resolution grids for each modelled object. Those high-resolution grids are moving with the objects through the simulation space (focused on the centre of density of an object). The resolution of the highest resolution grid has usually 67 pc per cell for the DM halo and 0.8 pc per cell for the SCs. This grid-level monitors the central area of the DM halo and the SCs, respectively. The mid-level grids have resolutions of 333 pc per cell for the halo and covers the complete area in which the SCs are moving and 166.6 pc for the SCs to resolve the interactions between the dissolving clusters properly. The outermost grid has the same size for all modelled objects and covers the simulation area beyond the virial radius of the DM halo, with a resolution for most simulations of about 1.6 kpc per cell. At a later stage of the simulation, when all SCs are dissolved and have formed a fuzzy luminous object, we re-order the stars into one luminous object with grid-sizes for the high-resolution grids depending on the size of the formed object. This is done for resolution and performance reasons, likewise.

The code uses a fixed time-step of 0.25 Myr to ensure that the internal dynamics of the initial clusters are resolved properly. We follow the evolution of our models over a long period of time, i.e. 10 Gyr and give the results of our models at the end of this time period. We study the final object by analysing its morphology, luminosity and dynamics.

One might argue that a particle-mesh code is not suitable to perform simulations of SCs as it is by definition collisionless and neglects internal two-body processes of the SCs, which are important for the long-term evolution of the cluster. But as almost all clusters in our simulations dissolve and spread their stars throughout the central region of the dwarf galaxy quite fast and we do not investigate the properties of surviving clusters, the stars in our simulations enter a collisionless state very quickly and are very well modelled by a collisionless code. As a final remark, we state that the star-particles in our simulations do not represent single stars at all. The particles of a mesh-based code rather represent tracers of the phase-space. Therefore, the actual number of star-particles does

not necessarily coincide with the number of stars. More information can be found in Fellhauer et al. (2000).

## 3 RESULTS

We perform 73 numerical simulations of which 53 simulations have different initial parameters. The 20 other simulations are repetitions of the same parameter sets with different random number seeds to analyse the importance of the low number statistics regarding the initial positions and velocities of our $N_0$ SCs. The goal is to show that our formation scenario of dSph galaxies leads to objects that resemble these galaxies, even when quite different initial conditions are assumed, thus demonstrating the plausibility of our scenario.

### 3.1 Surface density profile

Several surface density profiles have been used in the literature to fit the observed surface brightness curves of the dSph galaxies (Irwin & Hatzidimitriou 1995; Majewski et al. 2005). There is also some evidence of environmental effects in the surface brightness profiles of dSphs (Bellazzini, Fusi Pecci & Ferraro 1996; McConnachie & Irwin 2006; Read et al. 2006a). In this work, we consider Sérsic (Caon, Capaccioli & D'Onofrio 1993) profiles according to the following formula:

$$\Sigma(R) = \Sigma_{\rm eff} \exp\left(-b_n\left[\left(\frac{R}{R_{\rm eff}}\right)^{1/n} - 1\right]\right) \quad (2)$$

$$b_n = 1.9992n - 0.3271, \quad (3)$$

where $R_{\rm eff}$ is the effective radius and $\Sigma_{\rm eff}$ is the surface density at the effective radius. The index $n$ gives information about the shape of the dSph galaxy. In the case $n \approx 1$, we have an exponential-shaped profile for the surface density distribution.

Surface brightness profiles show integrated light along the line of sight. As we do not know along which line of sight our objects may be observed, we calculate a mean value out of three possible sight-lines along the Cartesian coordinate axes $x$, $y$ and $z$. Some of the simulations have been repeated using a different random number seed to explore the variations of the properties of the objects formed from different realizations of the same initial conditions.

The idea for considering Sérsic profiles comes from the fact that King profiles, even though widely used, do not reflect that we are analysing luminous components inside DM haloes, i.e. well shielded from any external potential. Therefore, the objects cannot be expected to be tidally truncated. Whereas some of the known dSph galaxies seem to be well fitted by King profiles, there is no physical reason behind it. We find that many of our models are not well fitted by King profiles with a truncation radius, i.e. a tidal radius. As our initial conditions for the stars are based on Plummer distributions, it is quite natural to try a Plummer fit to the results as well. Again, our results show that the luminous components are badly fitted by two-parameter Plummer profiles. This result can be seen as a confirmation that our choice of the initial distribution of the luminous mass does not affect the final outcome. Finally, the Sérsic profile has the advantage of being a three-parameter fit that easily adjusts to the data. A detailed overview of all profiles fitted to all the simulations can be found in Table A2.

In Fig. 1, we show the correlation between the three parameters of the Sérsic profile ($\Sigma_{\rm eff}$, $n$ and $R_{\rm eff}$) fitted to our models with the parameters $M_{500}$, $R_{\rm h}$ and $R_{\rm sc}$ of our initial conditions, while keeping the other two parameters constant. By analysing the data, we do not find any dependence of the Sérsic parameters on the halo profile used (Plummer or NFW) or on the number of SCs $N_0$. Also, as long as the SFE is low (i.e. 15 or 30 per cent), there is no dependence of the results either. We therefore calculate the mean values of the fitting parameters keeping the above-mentioned parameters constant but adding up all simulations with different profiles, number of SCs and SFE. The data points show the mean values and the error bars give the one sigma deviations of the mean.

In the left-hand column, we show the dependence of the Sérsic parameters on the mass of the halo within 500 pc. In these simulations, we keep $R_{\rm h} = 1.0$ kpc and $R_{\rm sc} = 0.25$ kpc constant. We do not see a change in the surface brightness profile parameters when changing the mass of the DM halo. One might expect more stars to settle in a deeper potential, but this seems not to be the case. Obviously, it is not the absolute value of the potential influencing the light distribution. This seems to be supported by observations, as we do not have large differences in surface brightness profiles between the dSph galaxies.

Instead, we do see a strong dependence of the effective surface brightness on the scalelength of the halo as seen in the top panel of the middle column of Fig. 1. The surface density increases as we go to smaller halo scalelengths. This can be understood as we have a steeper profile with smaller scalelengths. This contradicts in a sense our finding that we see no trend between cusped and cored profiles. But as the NFW profiles have a cusp in their centre, the Plummer profiles are steeper in the outer parts. We therefore conclude that it is rather a dependence on the steepness of the halo profile along all radii of the luminous component than just a function of the very central behaviour. Accordingly, if we distribute the mass more centrally concentrated, the scalelengths of the luminous components are slightly decreasing (bottom-middle panel).

Comparing our results with the classical dSph galaxies like Carina, Draco or Sextans (whose total luminous mass agrees with our fixed luminous mass), which have central surface-brightnesses of the order of 1–3 $L_\odot\,pc^{-2}$ (Irwin & Hatzidimitriou 1995, and references therein), our results favour larger halo scalelengths of approximately 0.5 kpc and more (taking into account that our effective brightness should be lower than the central one and that we expect a mass-to-light ratio, for the stellar component only, of larger than unity).

A strong rising trend of $R_{\rm eff}$ with $R_{\rm sc}$ is observed in the bottom-right panel of Fig. 1. This is also expected because if the luminous matter started more concentrated, it should also be more concentrated in the final object. For $R_{\rm sc} = 0.25$ kpc, the mean value of $R_{\rm eff}$ obtained in the simulations is $\bar{R}_{\rm eff} = 498 \pm 44$ pc. For $R_{\rm sc} = 0.5$ kpc the resulting objects have an average effective radius of $\bar{R}_{\rm eff} = 890 \pm 260$ pc. Finally, for simulations with an initial $R_{\rm sc}$ of 1 kpc, the final effective radius has a mean value of 1.45 kpc. Thus, the final scalelength is almost double the initial scalelength of the SC distribution. Here, the dependence of the effective surface density is not that pronounced but the dependence on the effective radius is quite strong.

The results show that we can disentangle the influence of the different initial parameters:

(i) the mass of the halo has no influence on the mean values of the Sérsic fits;

(ii) smaller scalelengths of the haloes lead to brighter dwarf galaxies in the central area and

(iii) if the luminous component is formed out of a smaller and denser gas-distribution (i.e. SC distribution), we see smaller scalelengths in our final galaxy.

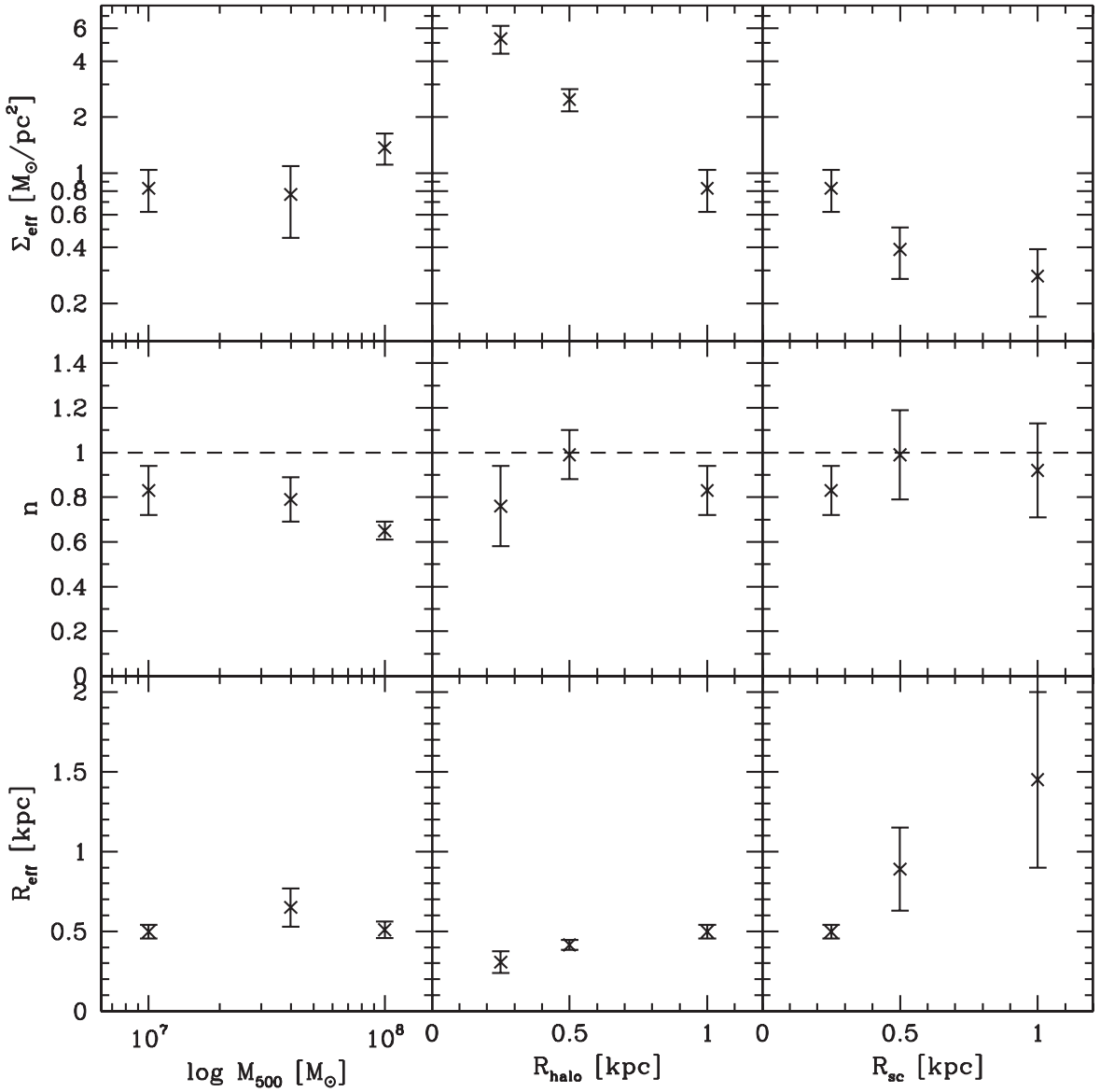


**Figure 1.** Correlation between the Sérsic parameters of our objects and the parameters of the initial conditions: $M_{500}$, $R_{\rm h}$ and $R_{\rm sc}$ keeping all other parameters constant. In the first column, we show the dependence of the Sérsic parameters as function of the mass of the halo within 500 pc. In these simulations, we keep all the other parameters constant, i.e. $R_{\rm halo} = 1.0$ kpc and $R_{\rm sc} = 0.25$ kpc. In the middle column, we show simulations whose $M_{500} = 1 \times 10^7\,{\rm M}_\odot$ and $R_{\rm sc} = 0.25$ kpc are kept constant and we vary the scalelength of the halo $R_{\rm h}$. In the right-hand column, we consider simulations with $M_{500} = 1 \times 10^7\,{\rm M}_\odot$ and $R_{\rm h} = 1.0$ kpc and vary the scalelength of the SC distribution $R_{\rm sc}$. The dashed line in the middle row shows $n = 1$, which corresponds to an exponential profile, as seen with spheroidal galaxies.

Another reassuring result is shown in the panels of the middle row of Fig. 1. We see that the Sérsic index $n$ has no dependence on any initial parameter. It shows always mean values around 1.0, independently of the values of $M_{500}$, $R_{\rm h}$ or $R_{\rm sc}$. This means that our resulting objects have approximately an exponential surface density profile, like the dSph galaxies of the Local Group (Caon et al. 1993; Jerjen, Binggeli & Freeman 2000; Walcher et al. 2003).

Photometrical observations of the dSph galaxies in the Local Group (Irwin & Hatzidimitriou 1995; Mateo 1998) show that we can find different sizes of these galaxies. For example, the effective radii of Draco, Ursa Minor, Sculptor and Fornax are 180, 200, 110 and 460 pc, respectively.

If our formation scenario is correct, then the initial distribution of baryons which now form the luminous components had smaller scalelengths in their initial gas distribution. As a rule by thumb, we can say: about half the value of their effective radii today.

### 3.2 Shape of the final objects in our simulations

It is possible to characterize the shape of our resulting objects considering the parameters of Clumpiness, $C$, introduced by Conselice (2003), the ellipticity $e$ of the object and the isophotal parameter $A_4$ (Khochfar & Burkert 2005). We show all results in Table A3.

#### *3.2.1 Clumpiness C*

One feature that can characterize the light distribution in a galaxy is the patchiness of the distribution. Conselice (2003) introduce the $C$-parameter (called clumpiness), which is a measure of the

inhomogeneity of the distribution of the stars. We deviate from the method explained in Conselice (2003) and construct a smooth elliptic model which fits our simulation results, using the IRAF routine ELLIPSE. Then, we subtract this smooth model from our data and sum the positive residuals. The ratio between these residuals and the original data is the clumpiness $C$. More details about this method can be found in Assmann et al. (2013).

In Fig. 2, we show the relationship between the clumpiness $C$ of the models and (top left) $M_{500}$, (top right) $N_0$, (bottom left) $R_h$ and (bottom right) $R_{sc}$. First, we observe that all our simulation lead to low values of the clumpiness parameter.

It is hard to compare our results with the classical dSph of the MW as there was not yet a determination of their clumpiness published. Comparing our results with values published in Conselice (2003), we see that our results for cuspy halo profiles and small halo scalelengths lie in the range of values found for dwarf ellipticals and the results for cored haloes and large scalelengths at the lower end of the values for dIrr.

10 Gyr of evolution are enough to erase almost all deviations from a smooth object in positional space. That this is not necessarily true for the velocity space will be dealt with in a later section.

In all panels, we observe that cored profiles (Plummer) lead to a higher clumpiness than the corresponding cusped profiles (NFW). This in fact is not a new result and was expected. Cuspy profiles are better in erasing substructure. Only if the scalelengths of the haloes are low, cuspy and cored profiles do not differ significantly any longer (see the bottom-left panel of Fig. 2). The mass of the halo (top left) and the scalelength of the SC distribution (bottom right) seem to have no influence on the clumpiness at all. Finally, we see a clear trend with the number of SCs (top right). If we distribute the mass into more SCs the resulting clumpiness is lower. This finding is expected as with an initial distribution which is 'smoother'

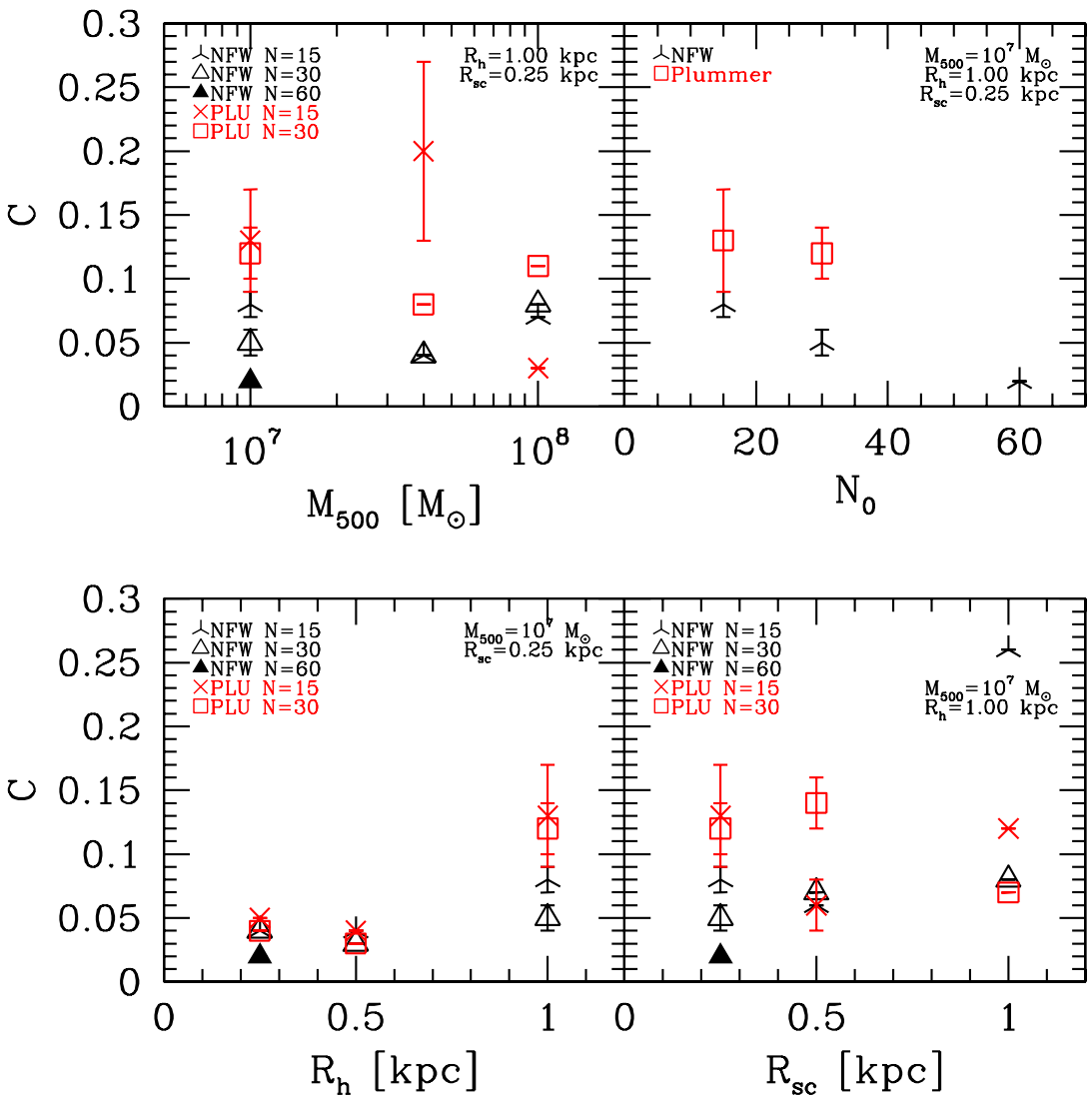


**Figure 2.** Dependence of the shape parameter clumpiness $C$. In all panels (black) tri-shaped symbols (three-pointed stars and triangles) represent simulations with NFW haloes. (Red) symbols with four corners (crosses and squares) belong to simulations using Plummer haloes. In all panels, except the top right, star symbols represent simulations using 15 SCs, open symbols represent 30 SCs and the filled symbol in the top left shows the result of the simulation using 60 SCs. In the top-left panel, the dependence on $M_{500}$ is shown. Here, we keep $R_h = 1.0$ kpc and $R_{sc} = 0.25$ kpc constant. The top right shows the dependence on the number of SCs $N_0$ keeping $M_{500} = 10^7$ M$_\odot$, $R_h = 1.0$ kpc and $R_{sc} = 0.25$ kpc constant. In the bottom-left panel, the dependence on the halo scalelength $R_h$ is shown keeping $M_{500} = 10^7$ M$_\odot$ and $R_{sc} = 0.25$ kpc constant. And in the bottom right, the dependence on the scalelength of the cluster distribution $R_{sc}$ is shown, again keeping $M_{500} = 10^7$ M$_\odot$ and $R_h = 1.0$ kpc constant. Symbols without error bars are based on a single simulation only.

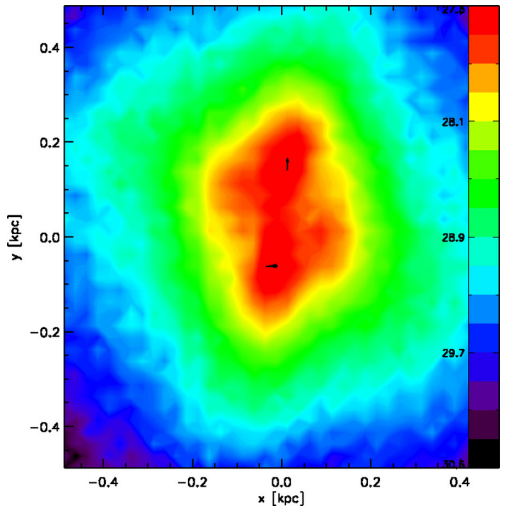


**Figure 3.** Surface brightness contours of the simulation with the most extreme deviation from ellipticity, i.e. the highest clumpiness.

one ends up with a final object which has less deviations from smoothness.

We can ask ourselves now, what does this 'clumpiness' mean for our resulting objects. We see a huge variety in shapes in our models, like off-centre nuclei, secondary density peaks, peanut-shaped central regions and as an extreme even two equally important density centres as shown as an example in Fig. 3.

### 3.2.2 *Ellipticity*

Another structural parameter is the ellipticity, $e$. This parameter is defined by

$$e = 1 - \frac{b}{a}, \tag{4}$$

where $b$ is the minor and $a$ is the major axis of an ellipse. The dSph galaxies of the Local Group Sculptor, Fornax, Ursa Minor and Draco have $e$ values of $0.32 \pm 0.03$, $0.31 \pm 0.03$, $0.56 \pm 0.05$ and $0.29 \pm 0.01$, respectively (Mateo 1998).

We determine the ellipticity values at the half-mass radius (as the ellipticity may vary throughout the dwarf) by fitting a smooth model to our simulation data using the IRAF routine ELLIPSE.

In the top row of Fig. 4, we study the dependence of $e$ on the initial parameters of our numerical experiments by keeping all other parameters constant. We observe no dependence between $e$ and $M_{500}$. In the first bin ($10^7$ M$_\odot$), we show two data points, for cusped and cored haloes separately, as we do have multiple realizations of those parameter sets to determine mean values and errors. As they agree (within $1\sigma$-error-bars), we do not distinguish between the two halo types. However, it is interesting to observe that the final objects have $e$ values close to the values of the classical dSph galaxies, regardless of whether the simulations had a cusped or cored DM halo (Mateo 1998; Martin, de Jong & Rix 2008; Sand et al. 2009, 2010; McGaugh et al. 2010; Munoz, Geha & Willman 2010).

It is also interesting that $e$ shows an increasing trend with the scalelength of the DM halo. At $R_\mathrm{h} = 0.25$ kpc, $e = 0.15 \pm 0.04$. When $R_\mathrm{h} = 0.5$ kpc, $e = 0.23 \pm 0.03$. Finally, for $R_\mathrm{h} = 1.0$ kpc, we show again the two separate results from the first panel and obtain $e = 0.27 \pm 0.06$ for NFW haloes and $e = 0.32 \pm 0.07$ for Plummer haloes. A possible explanation could be that with large scalelengths more mass of the halo is at larger radii and can influence radial orbits to be more eccentric, i.e. have larger apocentres. If now, due to our low number in SCs, more orbits are aligned in one direction leading to a non-spherical object, it will be even more elongated if we have a larger scalelength of the halo.

If this trend should be real in spite the large error bars, our data would suggest that the real dSph galaxies of the MW would have halo scalelengths preferably of 0.5 kpc or higher. This agrees well with our findings from the central surface-brightness.

There is no relation between the initial $R_\mathrm{sc}$ and the ellipticity of the final object (see the top-right panel).

### 3.2.3 $A_4$ *parameter*

Another parameter obtained from the ELLIPSE routine is the fourth-order Fourier-coefficient, $A_4$, which corresponds to the value of the isophotal deviation from a perfect ellipse. $A_4$ is positive for 'discy' galaxies and negative for 'boxy' galaxies (Khochfar & Burkert 2005). The results of all our simulations are shown in Table A3.

In the bottom row of Fig. 4, we show $A_4$ versus $M_{500}$, $R_\mathrm{h}$ and $R_\mathrm{sc}$. As always, we keep the other input parameter constant and only calculate the mean of simulations with identical initial conditions but different random seeds. In the figure, the parameter $A_4$, in general, tends to zero and this shows the spheroidal character of the objects. There is no observable trend between $A_4$ and $M_{500}$ or $R_\mathrm{h}$. As we can see in all panels (or better not see) is that the data points for cusped and cored haloes are almost identical and fall on top of each other. For $M_{500} = 10^7$ M$_\odot$, $R_\mathrm{h} = 1$ kpc and $R_\mathrm{sc} = 0.25$ kpc, we obtain for cusped haloes $A_4 = 0.010 \pm 0.025$ and for cored haloes $A_4 = 0.007 \pm 0.024$.

We do not believe that there is an actual trend to 'discy' shapes with high values of $R_\mathrm{sc}$. This data point is based on four simulations only, from which three show 'extreme' deviations from ellipticity. Such 'outliers' appear in every bin but usually with alternating signs. We think it is an effect by chance that for this data point all three 'outliers' have positive values.

The single values of the simulations are all in agreement with observations of elliptical galaxies (Bender, Döbereiner & Möllenhoff 1988). They all show only small deviations of the order of 0.01–0.1 with alternating signs, i.e. our formation process does favour neither discy nor boxy shapes.

### 3.2.4 *Surviving SCs*

We also indicate in Table A3 if we find SCs, which are not dissolved after the 10 Gyr of evolution in our simulations. We show these simulations also in Fig. 5 and plot the relative number of surviving SCs against the initial conditions of the simulations. We see in all panels that in cored haloes, clusters have a higher chance to survive. This suggests that travelling through a cuspy central region with small scalelength (i.e. steep potential gradient) does not enhance the survival-ability of the SCs. The bottom-left panel shows that more concentrated cluster distributions lead to more cluster surviving.

The bottom-right panel shows the obvious. If the SFE is as low as 15 per cent none of the cluster survives, independently how all other parameters are distributed. At an SFE of 30 per cent, we see that in some simulations we have a few cluster surviving the dissolution and destruction process, following the trends explained above. At an SFE of 60 per cent, we find the obvious result that none of the SCs gets disrupted. They are bound enough to survive their gas-expulsion and then the background potential is too strong, i.e. the clusters have too high encounter velocities, such that the SCs cannot merge.

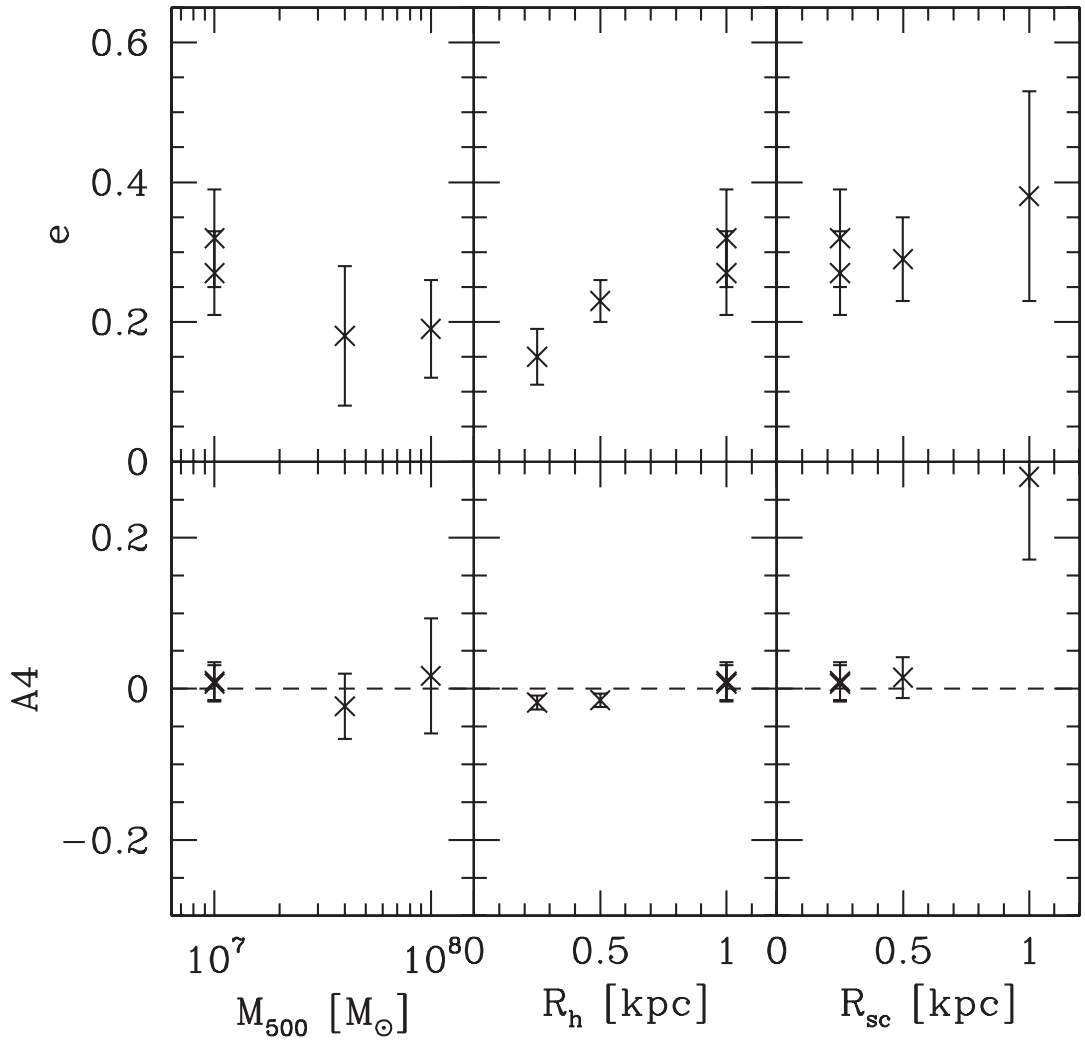


**Figure 4.** Ellipticity $e$ and isophotal deviation $A_4$ as function of the initial conditions $M_{500}$, $R_{\rm h}$ and $R_{\rm sc}$. In each panel, we vary one parameter and keep the other two constant at the values $M_{500} = 10^7\,{\rm M}_\odot$, $R_{\rm h} = 1.0\,{\rm kpc}$ and $R_{\rm sc} = 0.25\,{\rm kpc}$. The data points with exactly those values are split between cusped and cored haloes to show that the halo shape has no influence (the cored profiles have slightly higher $e$ but well within the error-bars and the results for $A_4$ are indistinguishable).

The surviving SCs are exclusively found in the very central areas at $r < 200\,{\rm pc}$. In the left-hand panel of Fig. 6, we show the surface brightness contours of a simulation, which hosts a surviving SC. The surviving SC is closely located to the centre. The simulation has a Plummer halo with a large scalelength of 1 kpc.

In the middle panels, we see the reason for its survival. In the top, we show its orbit which has an apocentre of only 200 pc. The lower panel shows the Lagrangian radii of this cluster. It expands due to the gas expulsion during the first few Myr but the expansion is halted and turned around after the SC reached its apocentre and continued orbiting towards the centre of the halo, i.e. particles, which were unbound and expanding get 'compressed' together again. After the pericentre passage, which corresponds also with the time, the particles have the smallest extension in space, the outer Lagrangian radii are re-expanding. With the 90 per cent radius reaching about 80 pc at the apocentre of 200 pc, those mass-shells are in reality unbound particles which follow the orbit of the original cluster and are sometimes closer to pericentre, together with the remaining centre of density of the SC and sometimes they are more distributed along the orbit at apocentre. But, the inner mass-shells (10 to 20 per cent of the initial mass) do not expand again after the first pericentre passage. They stay at an elevated but constant level and form the surviving SC.

To contrast these findings, we show in the right-hand panels the evolution of a dissolving SC. In the top panel, we see its orbit with pericentre and apocentre of 0.8 and 1.5 kpc respectively. Again, we see an initial expansion due to gas-expulsion in the first few Myr (in the scale of the figure almost invisible). Then, we see an oscillation in the Lagrangian radii as well. But, this oscillation happens on much larger scales and only reflects the fact that we have orbital crowding due to low orbital velocities of unbound particles at apocentre – therefore, we have the minima in the Lagrangian radii close to the apocentres – and very long tidal tails close to pericentre when the orbital velocities of the particles are high – therefore we see the maxima of the Lagrangian radii at or close to pericentre.

### 3.3 Velocity space

#### *3.3.1 Velocity dispersion*

We measure the line-of-sight velocity dispersion for the final objects to compare them with the typical value of about $10\,{\rm km\,s^{-1}}$ observed in classical dSph galaxies (Munoz et al. 2005).

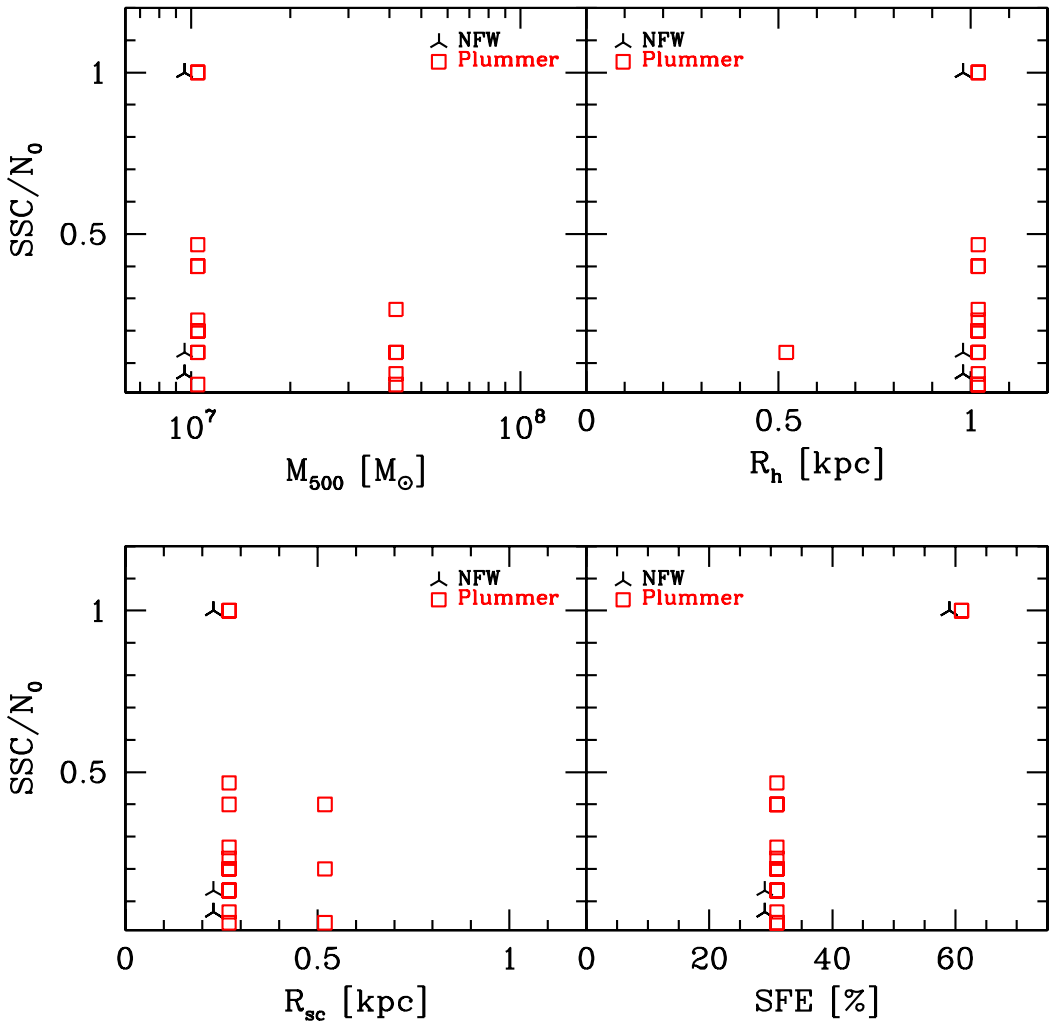


**Figure 5.** Surviving SCs for all our simulations as function of the initial parameters $M_{500}$, $R_{\rm h}$, $R_{\rm sc}$ and SFE. (Black) tri-pointed stars are simulations with a cuspy halo, and (red) open squares show simulations with a cored halo profile.

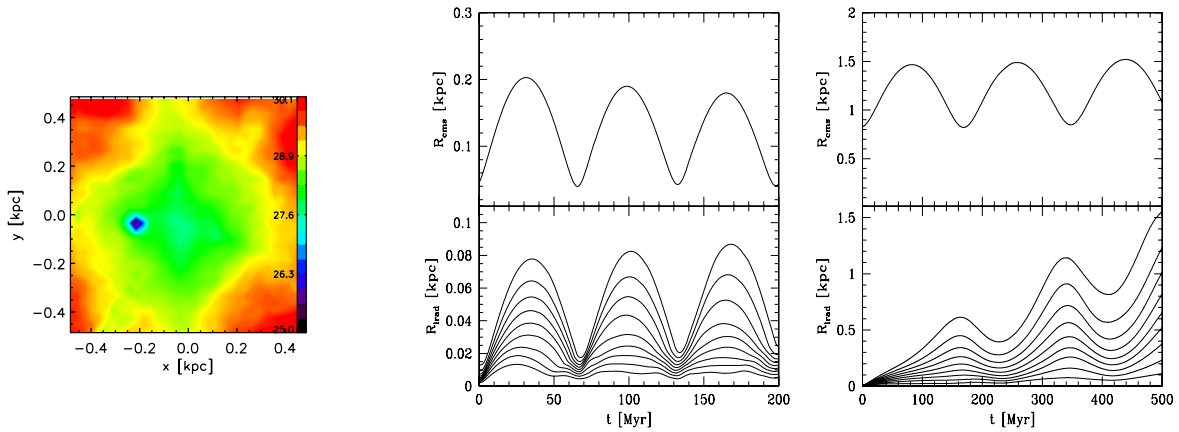


**Figure 6.** Why do SC survive? Left: surface brightness contours of a simulation showing a surviving SC in the central region. Middle: the top graph shows the distance to the centre of the halo of the surviving SC, while the lower graph shows the evolution of the Lagrangian radii (10, 20, . . . , 90 per cent of the mass) with time. Right: as a contrast, we show the same data as in the middle panel for a dissolving SC.

To measure the line-of-sight velocity dispersion of our models, we consider three different strategies. First, $\sigma_{0,\,\rm mean}$, where we consider the velocity dispersion of all particles within a projected radius of 10 pc from the centre of the object. The mean value is calculated by considering the mean of the values obtained along all three coordinate axis because the orientation of our objects is unknown. Further, we determine the radial profile of the line-of-sight velocity dispersion and fit a Plummer law to the data. From this fit,

we determine the central value $\sigma_{0,\,\mathrm{fit}}$. Finally, we calculate the velocity dispersion of all particles within a projected radius of 500 pc – $\sigma_{500}$. The values of these quantities can be found in Table A4. In this section, we will focus on discussing $\sigma_{500}$ and its relation to the initial parameters.

In the top row of Fig. 7, we show the dependence of $\sigma_{500}$ on the initial parameters of our models: $M_{500}$, $R_{\mathrm{h}}$ and $R_{\mathrm{sc}}$. In the top-left panel, we show the dependence on $M_{500}$. As expected, velocity dispersion increases with the mass of the DM halo. As mass (potential energy) is related to the square of the velocity (kinetic energy) we see this trend in our models as well. A bit puzzling are the results shown in the middle and right-hand panels. Theory of virial equilibrium predicts that

$$\sigma^2 \sim \frac{M_{\mathrm{dyn}}}{r_{\mathrm{scale}}}, \tag{5}$$

i.e. the velocity dispersion should decrease with increasing scalelength. This relation is true using the total dynamical mass (i.e. here the mass of the halo) and the velocity dispersion and scalelength of the tracer population, i.e. in our case $\sigma_{500}$ and $R_{\mathrm{eff}}$ of the final object. As we have shown in Fig. 1 that $R_{\mathrm{eff}}$ increases slightly with $R_{\mathrm{h}}$ and strongly with $R_{\mathrm{sc}}$, we would expect a decreasing trend in $\sigma_{500}$ with those two parameters as well. Instead, we see rather constant values for $\sigma_{500}$ as function of $R_{\mathrm{sc}}$ and even a slight increase (but within the errors) as function of $R_{\mathrm{h}}$.

This behaviour can be explained by an increase of velocity streams at larger scalelengths, stemming from the dissolved SCs. We will discuss these effects in a separate section below. Finally, we see no difference between cusped and cored haloes.

For DM haloes with masses of $M_{500} = 10^7\,\mathrm{M}_\odot$, the velocity dispersion of our final objects have similar values like the ones measured for some classical dSph galaxies (Munoz et al. 2005). For example: Carina, Leo II and Sextans have velocity dispersions around 7.0 km s$^{-1}$. This is in fact an interesting result. As Walker et al. (2007) claimed that almost all dwarfs galaxies should have a minimum DM halo mass of about $10^7\,\mathrm{M}_\odot$ within a radius of 300 pc, our models show that we can reach the same velocity dispersions with a lower halo mass.

Another consequence of our scenario is that objects formed in identical haloes can show slightly different velocity dispersions.

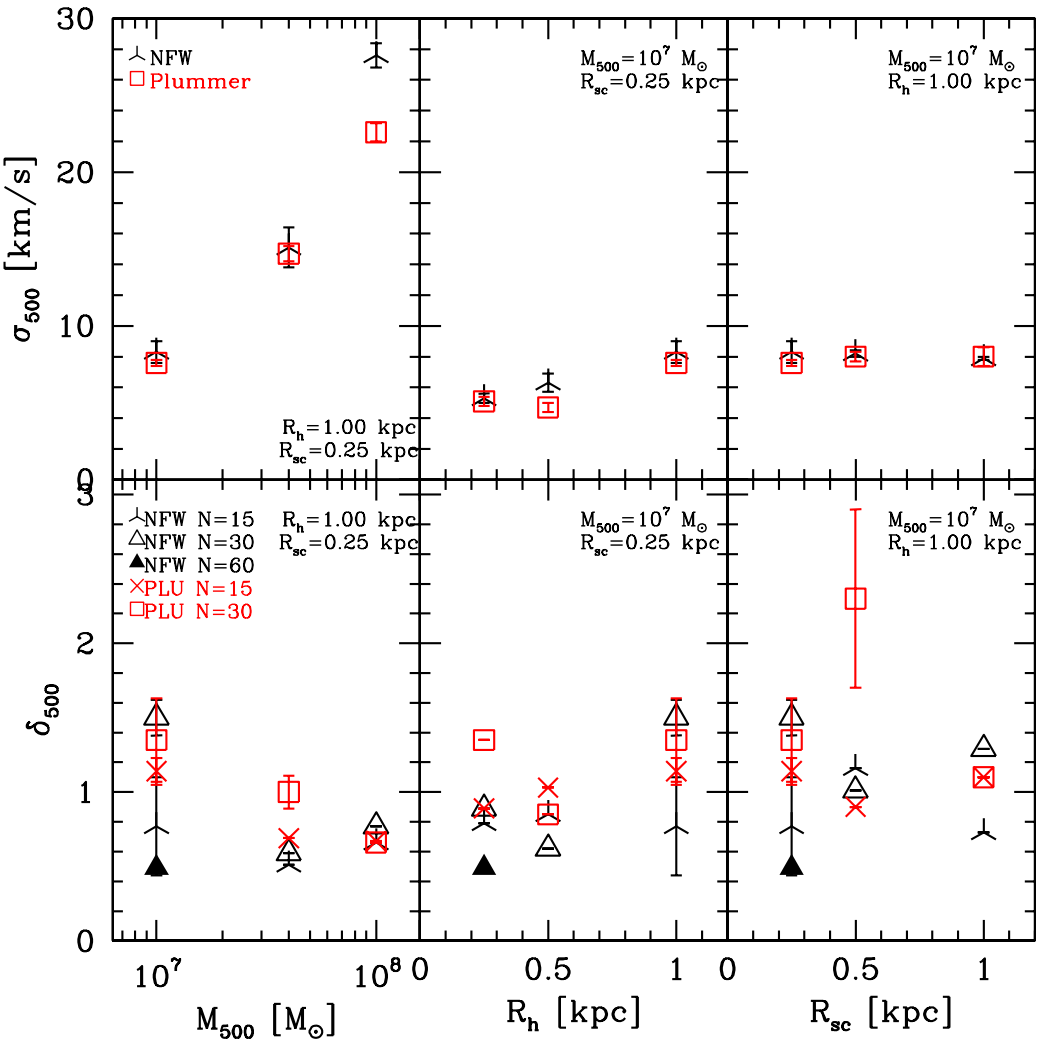


**Figure 7.** Line-of-sight velocity dispersion $\sigma_{500}$ (top row) and maximum deviation of the radial velocity $\delta_{500}$ (bottom row) as a function of the initial parameters of our models: $M_{500}$, $R_{\mathrm{h}}$ and $R_{\mathrm{sc}}$. In the top row, we show results for cuspy haloes as (black) tri-pointed stars and of cored haloes as (red) open squares. In the bottom row, we divide even further and show as (black) open triangles results of NFW haloes using $N_0 = 15$ SCs (black) tri-pointed stars show the NFW haloes with $N_0 = 30$ SCs and the filled triangle is the result of the $N_0 = 60$ simulation. (Red) open squares are Plummer haloes with $N_0 = 15$ and (red) crosses show Plummer haloes with $N_0 = 30$. As always we keep all other parameters constant as described in Fig. 2.

Otherwise we would have no error bars attached to our data points. The reason for this will become clear with the discussion of the results in the following subsection.

In Fig. 8, we show the line-of-sight velocity dispersion profiles for cusped (left-hand panels) and cored (right-hand panels) DM haloes for some of our simulations whose $M_{500} = 10^7\,\mathrm{M}_\odot$. These profiles have been obtained considering the mean value of the line-of-sight velocity dispersion within concentric rings of varying radius. From top to bottom, the scalelengths of the DM haloes are 1.0, 0.5 and 0.25 kpc, respectively. For both types of DM haloes, the velocity dispersion profiles obtained are always more or less flat.

Looking at the outer part of the profiles, we observe different types of behaviour in the dispersions. We get outer profiles (beyond 1 kpc) where the velocity dispersion falls slowly in some cases, while in others the dispersion stays flat. We see a similar behaviour in the MW's dwarf galaxies. In Sextans, we see a slight drop in velocity dispersion around 1 kpc, while Sculptor, Draco and Fornax show flat profiles (see fig. 2 in Walker et al. 2007).

In the intermediate part (0.1 to 1 kpc), some of our simulations show wiggles and bumps in the dispersion profile. While the observers always try to fit smooth curves, thus implicitly assuming that any bumps seen in the profiles are merely due to statistical noise (e.g. Sculptor, Draco or Carina) in our formation scenario these wiggles are real features. These deviations are due to artefacts in velocity space, we dubbed fossil remnants (see the following section). If our formation theory is true, the wiggles in the observed profiles might not be because of errors but they might be real features.

In the central part, we see the same behaviour as shown in the multitude of MW's dwarf galaxies. Some of our models have colder cores, i.e. their dispersion profile has a central dip like in Sextans or Draco (Munoz et al. 2005; Walker et al. 2007). Other models show a rising central velocity dispersion. We do not see a similar behaviour with the classical dSphs of the MW.

These results show clearly that our models are well suited to reproduce dSph galaxies. We reproduce the dynamics of the different dwarfs galaxies with our different models. In our models, the bumps in the observed profiles are not simply due to noise in the observed data sets. According to our formation theory they are a natural by-product of the formation scenario proposed in this work.

### *3.3.2 Fossil remnants*

In Fig. 9, we show the shape and dynamics of a representative example of our simulations within 500 pc as 2D pixel maps. As we are using more particles than actual stars, we are able to produce high-resolution 2D pixel maps not only of the surface brightness but also (as we know exactly the velocities of all particles) of the internal dynamics of the system.

In the left-hand panels, we show the surface brightness of the simulation N015M107RH100RS025S30 with a resolution of 25 pc.

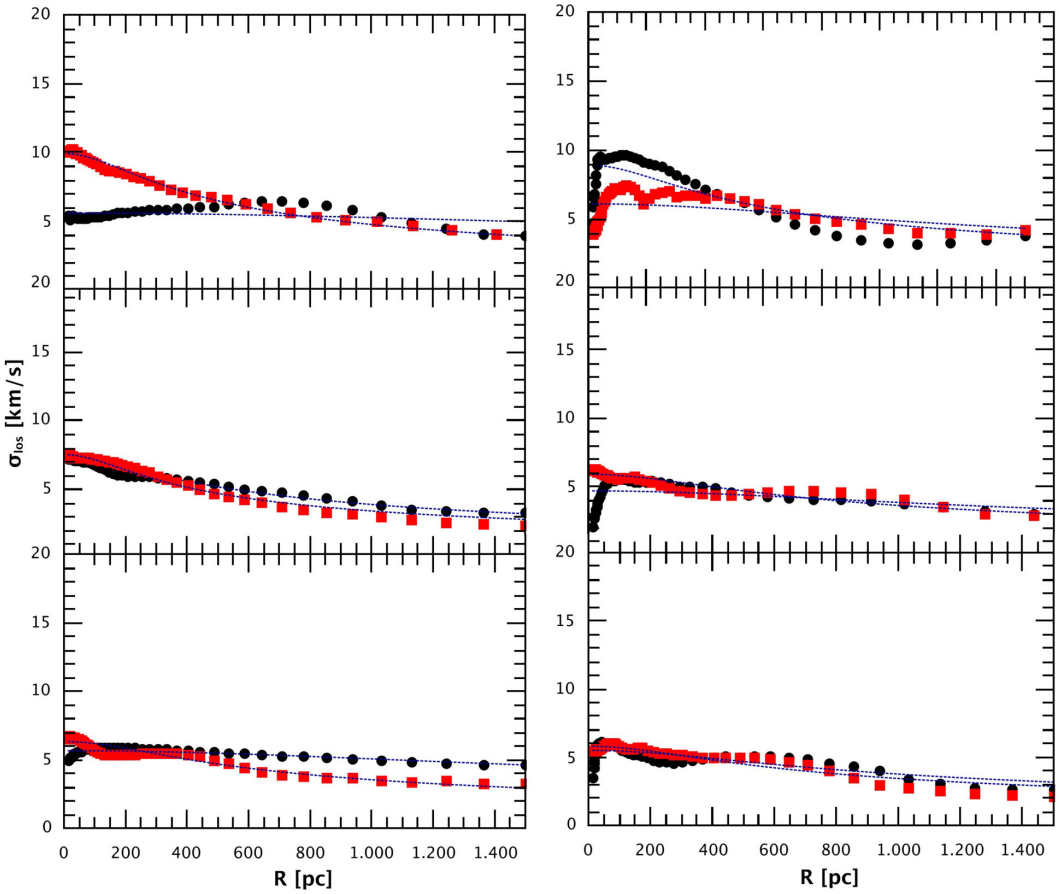


**Figure 8.** Line-of-sight velocity dispersion profiles for cusped (left-hand panels) and cored (right-hand panels) DM haloes for simulations with $M_{500} = 10^7\,\mathrm{M}_\odot$. From top to bottom, the scalelengths of the DM halo are 1.0, 0.5 and 0.25 kpc, respectively. Black and red colours correspond to simulations which initially have 15 or 30 SCs. Dashed lines are the fitting curves given by a Plummer fit to the data. For both types of DM haloes, the velocity dispersion profiles obtained are always more or less flat, out to large radii, as seen with dSph galaxies.

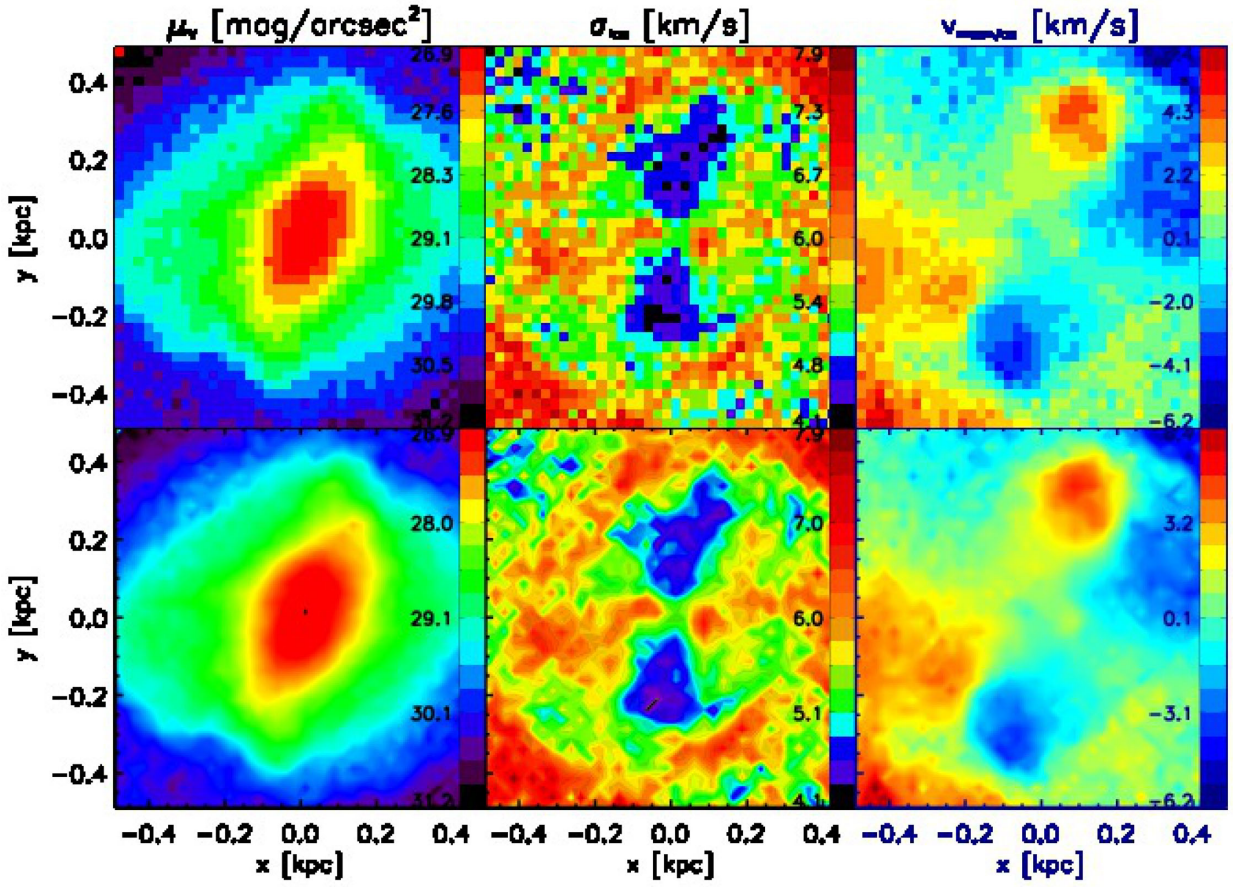


**Figure 9.** Shape and dynamics of simulation N015M107RH100RS025S30 within 500 pc as 2D pixel maps (top row) or as colour contours (bottom row). The pixel size is 25 pc. We show the surface brightness of our object in the left-hand panels (using an arbitrary mass-to-light ratio of $M/L = 1$ to convert masses in luminosities), the line-of-sight velocity dispersion calculated for each pixel in the middle panels and the mean velocity in each pixel in the right-hand panels.

These panels show, clearly, a centrally peaked and smooth density distribution for the luminous component of our final object. This distribution differs from our fiducial model (Assmann et al. 2013), indicating that the number of initial SCs can affect the final properties of the dSph galaxies. However, the fact that a simulation with a lower number of SCs forms a smoother surface density distribution is not due to some unknown and implausible physical effect; it is simply the result of the strong randomness of our results. The final details of our models not only depend on the initial parameters, but they are also strongly dependent on the random placements and orbits of the initial SCs. As we are using only 15–60 SCs in our models, it is clear that the detailed results are highly dependent on the random realization of those few clusters. In the previous sections, we tried to overcome this randomness by calculating mean values taken from many simulations of the same type.

In the middle-column of Fig. 9, we show the line-of-sight velocity dispersion calculated for each pixel separately. We see regions with cold velocities of around 4.5 km s$^{-1}$ in two opposing regions, almost but not perfectly aligned with the major axis of the dwarf. In the outskirts, the velocity dispersion increases. But the distribution of the velocity dispersion is far from being smooth. One can, clearly, observe substructures that are not present in the surface brightness plots. While the DM halo was able to erase the substructures in position space; substructures survive in velocity space. We refer to these substructures in velocity space, which remain after the formation process of our objects, as 'fossil remnants'. In all of our simulations, we observe these substructures in velocity space.

In the right-hand panels of Fig. 9, we show the mean velocity of all particles within a pixel. These figures show regions of coherent streaming motions with velocity differences of up to 4 km s$^{-1}$. The presence of streaming motions means that there are groups of stars, of dissolved clusters, that are trapped in the potential well of the halo at uniform motion. It is possible to observe at least two ring-like structures of opposing radial velocities. This type of scenario has been considered, recently, to explain the velocity distribution of the UMi dSph galaxy (Kleyna et al. 2003). The reason why we should expect to observe these ring structures, in velocity space, is that the dSph galaxies are faint objects with a low number density of stars; therefore, even a few stars on a similar orbit can produce a detectable signal. Of further interest is that the features in the mean velocity do not necessarily coincide with features we see in the dispersion map. In Assmann et al. (2013), we showed that the boosted velocity dispersions stem from distributions which are highly non-Gaussian, because they are in fact the overlay of stars on different orbits of the initial SCs.

Our model shows that ring structures are present even after 10 Gyr, and this is physically expected due to the long relaxation times of the stars in dwarf galaxies. That ring structures are formed from SCs on more circular orbits, which spread their stars slowly along the orbit. In the case that the SC have radial orbits, they will tend to disperse, since they will interact with other clusters in the

centre of the halo or with the central cusp. Thus, the ring structure should not be within the central area of the galaxy and should expand during the evolution of the dwarf galaxy.

An important consequence of having streaming motions in dwarf galaxies is the fact that it implies, if not properly taken into account, an overestimation of the velocity dispersion. This is the reason why we need less DM (than models which are featureless and in equilibrium) in our scenario to explain the velocity dispersions typical of observed dSph galaxies.

To quantify the strength of the streaming motions in the objects, we introduce the $\delta$-parameter:

$$\delta = \frac{\left|v_{\mathrm{mean,pixel}} - v_{\mathrm{mean,object}}\right|}{\sigma_{500}}. \quad (6)$$

The advantage is that it shows regions where the deviation of the mean velocity is distinct from zero. Higher values of $\delta$ correspond to regions where the streaming motions are strong. If no streaming motions are present, the $\delta$-parameter is randomly distributed without correlations. Also it is easily shown by means of basic statistics or Monte Carlo simulations (Fellhauer 2012) that the maximum value of $\delta$ due to random effects only depends on the number of velocities you use to calculate the mean. Random deviations of the calculated mean velocity from the 'true value' due to low number statistics on a three-sigma level lead to $\delta$ values of 1.25 for 10 stars, 0.4 for 100 stars and 0.14 for 1000 stars, i.e. measurements. As said before, we have an oversampling of particles in our simulations and the pixels in Fig. 10 and 9 contain 300 particles or more. So all the velocity features we see are real and not due to low numbers. In these high-resolution plots, we have 300–3000 particles in each pixel so as a conservative number whenever $\delta > 0.3$, the streaming motions are real and not due to random sampling.

In Fig. 10, we show the $\delta$ distribution for the same simulation as shown in Fig. 9. Once again a clear sign that we are dealing with coherent motions and not random deviations is that we see regions spanning many pixel showing similar high $\delta$ values. The imaginary figure 8 with low values has no special meaning and is rather a matter of contingency.

The maximum value of $\delta$ found in a single pixel within a region of radius 500 pc we call $\delta_{500}$. It is a measure of the strength of the velocity deviations in our models and allows us to compare the simulations with each other. The values are given in Table A4.

If we analyse the dependences of $\delta_{500}$, we see in the bottom panels of Fig. 7 that we have no dependence of this parameter with the mass of the halo (except maybe that we see less scatter in the results at higher masses) or with the scalelength of the SC distribution. We see that the majority of symbols representing cored Plummer haloes are above the corresponding NFW haloes meaning that cusped halo profiles seem to be better in erasing kinematical substructure (i.e. fossil remnants). But that would imply that we should also see a dependence with the halo scalelength, meaning larger scalelengths lead to higher values. This behaviour is not visible in our data, although three out of four data points for $R_{\mathrm{h}} = 1.0$ kpc lie above $\delta_{500} = 1.0$, while for the other scalelengths only one out of four is above this value.

We also cannot identify a dependence on the number of SCs as long as the numbers are low (i.e. $N_0 = 15, 30$). If we use $N_0 = 60$, we see the lowest value of $\delta_{500}$. We conclude that we would need to distribute the luminous mass into a real high number of low-mass SCs to really see a strong dependence on $N_0$, meaning that $\delta_{500}$ tends to zero, i.e. is below the stochastic noise.

While we have shown in Assmann et al. (2013) that in reality even with more than 2000 radial velocities observed it is still almost impossible to detect the fossil remnants in low-resolution 2D plots, they have visible counterparts in the 1D bumps and wiggles of the radial profiles. Of course we average the high discrepancies out by taking means over a whole radial ring but some small deviations remain visible. As already pointed out in Assmann et al. (2013), these bumps and wiggles are present in the observational data but are regarded as statistical noise as they are smaller than the errors. We see the same behaviour in our models and these deviations are real.

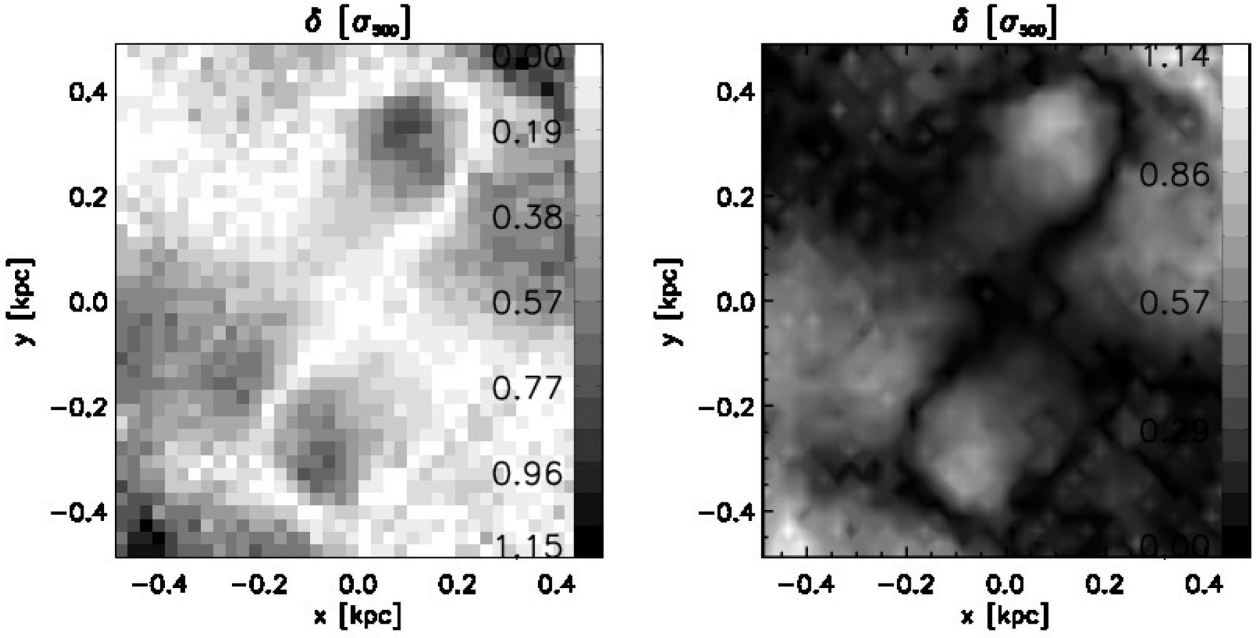


**Figure 10.** $\delta$-parameter distribution for the simulation N015M107RH100RS025S30. Left-hand panel shows the pixel map and right-hand panel the contours now with inverted grey-scale. The resolution is 25 pc per pixel.

## 4 DISCUSSION

Our initial conditions assume that the SCs are initially distributed according to a non-rotating Plummer profile within the dSph halo. Whether this is a realistic assumption or whether we should instead consider an initial distribution with non-zero angular momentum is an open question. However, we note that the hierarchical merger process through which dSphs acquire their DM and gas at high redshift are very violent and it is therefore likely that star formation, when it occurs, takes place before the gas distribution has time to settle into a rotationally supported disc. Even if such a disc were to form, observations show that the molecular and atomic gas of disc galaxies generally has velocity dispersions higher than $5\,\mathrm{kms}^{-1}$ (Stark & Brand 1989; Tamburro et al. 2009) which is taken to indicate the presence of gas turbulence. Given that such turbulent gas velocities are similar to the velocity dispersion in a dSph, any disc which formed would likely have a scaleheight to scale-radius of order unity and therefore not be very dissimilar to our assumed spherical initial conditions (e.g. Read, Pontzen & Viel 2006b)

We also note that the Leo T dwarf galaxy has a gas disc which displays negligible rotation and therefore constitutes an example of a system with little or no primordial angular momentum, but sufficient gas to support further star formation. Our models are thus directly relevant for an object such as Leo T, as well as any systems with more spheroidal gas distributions. Given that the SCs in our simulations are initially expanding due to gas expulsion, it is possible that our models would yield dSphs with little or no angular momentum, even if the initial configuration of the clusters were disc-like and contained some angular momentum. We intend to explore such initial conditions in a future paper.

Finally, we note that given the relatively short crossing-time within the dSph halo, as well as the low SFE within the SCs, the final distribution of the luminous component of our remnants is relatively insensitive to the initial spatial distribution we assume. In particular, Plummer profiles do not yield good fits to the final stellar distributions of our final objects, demonstrating that the merger process has erased much of the original configuration. Thus, our assumption of a particular form for the distribution of our clusters has little impact on the properties of the dSphs we form.

The question remaining is: are such velocity structures, as predicted by our formation scenario, present and observable in real dSph galaxies. If we have sufficient radial velocity measurements, we can calculate similar 2D maps like in our simulations. We do not expect, in the near future, to have a sufficient pixel-resolution with real observations to see coherent structures, i.e. many pixels with the same motion next to each other. But any sign of symmetry of pixels with high $\delta$ would be a good indicator. If we look at the maximum $\delta$-values obtained in our simulations, we deduce, that as soon as we have observational pixel maps with 50–100 stars per pixel almost all the 'real' $\delta$-values from the coherent motions in our simulations should be detectable. The strongest values of $\delta$, we detect in our simulations, could even be visible if small enough pixels with 10–20 stars only are observed.

Since we are considering that the final objects of our models resemble dSph galaxies, and thus that our formation scenario corresponds to the formation scenario of dSph galaxies, it is legitimate to ask if such streaming motions could be present in known dSph galaxies. Some of the classical dSph galaxies of the Local Group have now more than 2000 radial velocities measured and the first low-resolution pixel maps of the velocities should be feasible to produce in the near future.

It is known that Ursa Major II and Hercules show strong velocity gradients of 7–14 km s$^{-1}$. If these measurements are not due to tidal distortion, we estimate that these gradients correspond to values of $\delta > 0.5$, which is in accordance with most of the $\delta$-values obtained in our models.

Another important point to observe from our results is the fact that low SFE (SFE $\leq 30$ per cent) is necessary to obtain our objects. That is, low SFE lead to subsequent dissolution of the initial SCs. Only in this case we get sufficiently low phase-space densities of the luminous components that resemble dSph galaxies. Merging SCs without expansion always lead to compact objects, even without the presence of a DM halo (Fellhauer & Kroupa 2002).

As mentioned before, there are simulations where some of the initial SCs survive. In these cases, the SCs escaped from the dissolution process by experiencing a compressing force in the central region of the halo, allowing the cluster to stay bound. We find these SCs on orbits which never leave the central region of the luminous component of the dwarf galaxies.

The survival of the SCs seems to be completely random in our simulations, that is, it does not seem to depend on the initial parameters $M_{500}$, $R_{\rm h}$ or $R_{\rm sc}$. But, we do see more survivors in cored than in cusped haloes. A flat central density structure seems to act in favour of constructive compression than of destructive tidal forces.

Still this mechanism cannot explain the presence of globular clusters associated with dSph galaxies like Fornax. We strongly believe that those clusters, outside or in the outer parts of the luminous components, must have formed with high SFEs, which allowed them to survive in the first place. We see this behaviour in our simulations with an artificial high SFE of 60 per cent, in which all of our SCs are still present even after 10 Gyr of evolution, i.e. the tidal forces of the dSph galaxy are not sufficient to disrupt those clusters completely (note that our code cannot model any internal evolution due to two-body effects inside the SCs). That is, our simulations provide a straightforward solution to why some dSph galaxies have orbiting SCs and why some (most) of them do not.

Finally, we have to admit that most of our trends are still based on low number statistics. Even though this study is based on more than 60 simulations, using random placements of only 15 or 30 SCs can largely affect the outcome of a single simulation. We would need a much larger sample sizes of simulations for each set of initial parameters to be more confident in our trends. Nevertheless, those trends would still only provide a prediction in a statistical sense and we would be able to deduce the most likely initial parameters of a real dSph galaxy only.

## 5 CONCLUSIONS

In this work, we propose and test a new scenario for the formation of dSph galaxies. The scenario is based on two standard theories. We consider that stars never form in isolation but in SCs which suffer from gas expulsion. We also base our model on the widely accept $\Lambda$CDM cosmological model, where it is assumed that small DM haloes form first. We propose that the dynamical evolution of SCs, i.e. their dissolution due to gas expulsion in the centre of small DM haloes, may explain the formation of classical dSph galaxies. In our scenario, we simulate a DM halo with SCs inside. These SCs have low SFE and, thus, are designed to dissolve inside the DM halo forming the luminous components of the dSph galaxy. We follow the evolution of the SCs within the DM halo for 10 Gyr and measure the properties of the objects formed.

In this work, we perform an investigation of the vast possible parameter space and study how the morphology, luminosity and velocity space of the final objects are affected by the initial conditions of the simulations. In our experiments, we take cusped and cored DM haloes into account, and study, for each type of DM halo, how different mass distributions, number of interacting SCs, SFEs and initial distributions of the interacting SCs can affect the formation process of the dSph galaxies.

Regarding the light distribution, we see the following trends in our simulations: a decrease of effective surface brightness with larger halo scalelengths and an increase of the effective radius of the luminous component with increasing scalelength of the initial SC- and/or gas-distribution. We can identify two rules of thumb. To reach similar low brightnesses as seen in Carina, Draco and Scupltor our models favour larger scalelengths of the halo, i.e. $>500$ pc. Another trend is that the effective radius of the luminous object is almost twice as large as the initial scalelength of the SC distribution.

Even though our model starts out initially very 'clumpy', i.e. the stars are distributed in SCs, we obtain smooth models at the end of the evolution. Although relaxation times are long, the stars settle into a more or less smooth object. Of course we find that cored haloes are better in preserving some 'clumpiness' than cusped haloes.

The objects have internal structures within 500 pc that have an observable luminosity comparable to the luminosity of dSph galaxies. They also have similar morphological parameters. One interesting result from our simulations is that even 10 Gyr of evolution is not enough to destroy all substructures that stem from the formation process of our models.

Even though we start out with spherical distributions of the SCSs, our final luminous object has ellipticities similar to those observed with the classical dwarf galaxies. Again, we see a trend that larger scalelengths of the haloes lead to higher ellipticities.

In velocity space, the final objects have overall properties similar to typical classical dSph galaxies. We show that the velocity dispersions are around 5–10 $\mathrm{km\,s^{-1}}$ for halo masses of $M_{500} = 10^7\,\mathrm{M}_\odot$ and that the velocity dispersion profiles do not fall sharply at large radii, which is an indication of DM dominated objects as it is the case of dSph galaxies.

As a final result, we observe in the velocity space of our models some fossil remnants of the formation process, which give predictions for dynamical observations that could be used for validating our scenario about the formation of the dSph galaxies. We show the existence of streaming motions even after 10 Gyr of evolution, irrespective of halo mass, shape or scalelength. With the larger-than-life resolution we have in our simulations, we can visualize these streams in form of 2D-contour plots of the dispersion and the mean velocity. Observationally, this is still impossible. But, we show that these velocity deviations are still visible, if averaged in radial bins. Then, these deviations produce wiggles and bumps in the profile, similar to the observed profiles of the classical dwarfs.

## ACKNOWLEDGEMENTS

PA thanks the support of CONICYT PhD scholarship, BASAL PFB-06/2007, PROYECTO FONDAP 15010003 and the travel grant MECESUP-FSM0605. We also thank W. Dehnen for his help with the NFW profiles and P. Kroupa for enlightening discussions. MF acknowledges financial support of FONDECYT grant nos 1095092 and 1130521 and BASAL PFB-06/2007. MIW acknowledges the Royal Society for support. RS acknowledges financial support of FONDECYT grant no. 3120135.

## REFERENCES

Aarseth S. J., Henon M., Wielen R., 1974, A&A, 37, 183
Assmann P., Fellhauer M., Wilkinson M. I., Smith R., 2013, MNRAS, 432, 274
Battaglia G., Helmi A., Tolstoy E., Irwin M., Hill V., Jablonka P., 2008, ApJ, 681, L13
Battaglia G., Tolstoy E., Helmi A., Irwin M., Parisi P., Hill V., Jablonka P., 2011, MNRAS, 411, 1013
Bellazzini M., Fusi Pecci F., Ferraro F. R., 1996, MNRAS, 279, 337
Bellazzini M., Ferraro F. R., Pancino E., 2001, MNRAS, 327, L15
Belokurov V. et al., 2006, ApJ, 647, L111
Belokurov V. et al., 2007, ApJ, 654, 897
Bender R., Döbereiner S., Möllenhoff C., 1988, A&AS, 74, 385
Binney J., Tremaine S., 1987, Galactic Dynamics. Princeton Univ. Press, Princeton, NJ
Bressert E. et al., 2010, MNRAS, 409, L54
Caon N., Capaccioli M., D'Onofrio M., 1993, MNRAS, 265, 1013
Cole D., Dehnen W., Read J., Wilkinson M. I., 2012, MNRAS, 426, 601
Coleman M., Da Costa G. S., Bland-Hawthorn J., Martínez Delgado D., Freeman K. C., Malin D., 2004, AJ, 127, 832
Coleman M. G., Da Costa G. S., Bland-Hawthorn J., Freeman K. C., 2005, AJ, 129, 1443
Conselice C. J., 2003, ApJS, 143, 1
Dehnen W., McLaughlin D. E., 2005, MNRAS, 363, 1057
Del Popolo A., 2012, MNRAS, 419, 971
D'Onghia E., Besla G., Cox T., Hernquist L., 2009, Nat, 460, 605
Einasto J., Saar E., Kaasik A., Chernin A. D., 1974, Nat, 252, 111
Faber S. M., Lin D. N. C., 1983, ApJ, 266, L17
Fall S. M., 2006, ApJ, 652, 1129
Fellhauer M., 2012, Bol. Assoc. Argentina Astron., 54, 155
Fellhauer M., Kroupa P., 2002, MNRAS, 330, 642
Fellhauer M., Kroupa P., Baumgardt H., Bien R., Boily C. M., Spurzem R., Wassmer N., 2000, New Astron., 5, 305
Gilmore G., Wilkinson M., Kleyna J., Koch A., Evans W., Wyse R. F. G., Grebel E. K., 2007, Nucl. Phys. B, 173, 15
Gnedin O. Y., Hernquist L., Ostriker J. P., 1999, AJ, 514, 109
Goerdt T., Moore B., Read J. I., Stadel J., Zemp M., 2006, MNRAS, 368, 1073
Grcevich J., Putman M. E., 2009, ApJ, 696, 385
Irwin M., Hatzidimitriou D., 1995, MNRAS, 277, 1354
Irwin M. J. et al., 2007, ApJ, 656, L13
Jerjen H., Binggeli B., Freeman K. C., 2000, AJ, 119, 593
Kazantzidis S., Lokas E. L., Callegari S., Mayer L., Moustakas L. A., 2011, ApJ, 726, 98
Khochfar S., Burkert A., 2005, MNRAS, 359, 1379
Kleyna J. T., Wilkinson M. I., Gilmore G., Evans N. W., 2003, ApJ, 588, L21
Kleyna J. T., Wilkinson M. I., Evans N. W., Gilmore G., 2004, MNRAS, 354, L66
Klimentowski J., Lokas E. L., Kazantzidis S., Mayer L., Mamon G. A., 2009, MNRAS, 397, 2015
Kormendy J., Bender R., 2012, AJ, 198, 2
Kravtsov A. V., Gnedin O. Y., Klypin A. A., 2004, ApJ, 609, 482
Lada C. J., Lada E. A., 2003, ARA&A, 41, 57
McConnachie A., Irwin M., 2006, MNRAS, 365, 1263
McGaugh S. S., Schombert J. M., de Blok W. J. G., Zagursky M. J., 2010, ApJ, 708, L14
Mackey A. D., Gilmore G. F., 2003, MNRAS, 340, 175
Majewski S. et al., 2005, AJ, 130, 2677
Martin N. F., de Jong J. T. A., Rix H.-W., 2008, ApJ, 684, 1075
Mayer L., Governato F., Colpi M., Moore B., Quinn T., Wadsley J., Stadel J., Lake G., 2001, ApJ, 559, 754
Mayer L., Mastropietro C., Wadsley J., Stadel J., Moore B., 2006, MNRAS, 369, 1021
Mayer L., Kazantzidis S., Mastropiero C., Wadsley J., 2007, Nat, 445, 738
Mateo M. L., 1998, ARA&A, 36, 435
Metz M., Kroupa P., Jerjen H., 2007, MNRAS, 374, 1125

Munoz R. R. et al., 2005, ApJ, 631, L137
Munoz R. R., Geha M., Willman B., 2010, AJ, 140, 138
Navarro J. F., Frank C. S., White S. D. M., 1997, ApJ, 490, 493 (NFW)
Plummer H. C., 1911, MNRAS, 71, 460
Read J. I., Wilkinson M. I., Evans N. W., Gilmore G., Kleyna J. T., 2006a, MNRAS, 367, 387
Read J. I., Pontzen A. P., Viel M., 2006b, MNRAS, 371, 885
Ryan-Weber E. V., Begum A., Oosterloo T., Pal S., Irwin M. J., Belokurov V., Evans N. W., Zucker D. B., 2008, MNRAS, 384, 535
Sand D. J., Olszewski E. W., Willman B., Zaritsky D., Seth A., Harris J., Piatek S., Saha A., 2009, ApJ, 704, 898
Sand D. J., Seth A., Olszewski E. W., Willman B., Zaritsky D., Kallivayalil N., 2010, ApJ, 718, 530
Sakamoto T., Hasegawa T., 2006, ApJ, 653, L29
Simon J. D., Geha M., 2007, ApJ, 670, 313
Stark A. A., Brand J., 1989, ApJ, 339, 763
Tamburro D., Rix H.-W., Leroy A. K., Mac Low M.-M., Walter F., Kennicutt R. C., Brinks E., de Blok W. J. G., 2009, AJ, 137, 4424
Tutukov A. V., 1978, A&A, 70, 57
Walcher C. J., Fried J. W., Burkert A., Klessen R. S., 2003, A&A, 406, 847
Walker M. G., Peñarrubia, 2011, ApJ, 742, 20
Walker M. G., Mateo M., Olszewski E. W., Pal J. K., Sen B., Woodroofe M., 2006, ApJ, 642, L41
Walker M. G., Mateo M., Olszewski E. W., Gnedin O. Y., Wang X., Bodhisattva S., Woodroofe M., 2007, ApJ, 667, L53
Whitmore B. C., Zhang Q., Leitherer C., Fall S. M., Schweizer F., Miller B. W., 1999, AJ, 118, 1551
Wilkinson M. I., Kleyna J., Evans N. W., Gilmore G., 2002, MNRAS, 330, 778
Willman B. et al., 2005, ApJ, 626, L85
Zucker D. B., 2006, ApJ, 643, L103

## SUPPORTING INFORMATION

Additional Supporting Information may be found in the online version of this article:

**Table A1.** Table summarizing the initial parameters of our simulations.
**Table A2.** Results of the surface density profiles fitted to each simulation.
**Table A3.** The morphological parameters for the final objects of each simulation.
**Table A4.** Table of all results regarding the velocity dispersion and $\delta$-parameter (http://mnras.oxfordjournals.org/lookup/suppl/doi:10.1093/mnras/stt1448/-/DC1).

Please note: Oxford University Press are not responsible for the content or functionality of any supporting materials supplied by the authors. Any queries (other than missing material) should be directed to the corresponding author for the article.

This paper has been typeset from a TEX/LATEX file prepared by the author.